SANDIA REPORT
SAND2001-0661
Unlimited Release
Printed March 21

Computer Simulation of Bubble Growth in Metals Due to He

Stephen M. Foiles and Jeff J. Hoyt

Prepared by
Sandia National Laboratories
Albuquerque, New Mexico 87185 and Livermore, California 94550

Sandia is a multiprogram laboratory operated by Sandia Corporation, a Lockheed Martin Company, for the United States Department of Energy under Contract DE-AC04-94AL85000.

Issued by Sandia National Laboratories, operated for the United States Department of Energy by Sandia Corporation.

Available to DOE and DOE contractors from
U.S. Department of Energy
Office of Scientific and Technical Information
P.O. Box 62
Oak Ridge, TN 37831

Telephone: (865)576-8401
Facsimile: (865)576-5728
E-Mail: reports@adonis.osti.gov
Online ordering: http://www.doe.gov/bridge

Available to the public from
U.S. Department of Commerce
National Technical Information Service
5285 Port Royal Rd
Springfield, VA 22161

Telephone: (800)553-6847
Facsimile: (703)605-6900
E-Mail: orders@ntis.fedworld.gov
Online order: http://www.ntis.gov/ordering.htm

SAND2001-0661
Unlimited Release
Printed March 2001

Computer Simulation of Bubble Growth in Metals Due to He

Stephen M. Foiles and Jeff J. Hoyt
Science-Based Materials Modeling Department
Sandia National Laboratories
P.O. Box 5800
Albuquerque, NM 87185-1411

Abstract

Atomistic simulations of the growth of helium bubbles in metals are performed. The metal is represented by embedded atom method potentials for palladium. The helium bubbles are treated via an expanding repulsive spherical potential within the metal lattice. The simulations predict bubble pressures that decrease monotonically with increasing helium to metal ratios. The swelling of the material associated with the bubble growth is also computed. It is found that the rate of swelling increases with increasing helium to metal ratio consistent with experimental observations on the swelling of metal tritides. Finally, the detailed defect structure due to the bubble growth was investigated. Dislocation networks are observed to form that connect the bubbles. Unlike early model assumptions, prismatic loops between the bubbles are not retained. These predictions are compared to available experimental evidence.

Introduction:

The accumulation of helium in metals or metal tritides is known to result in the formation of helium bubbles in the lattice and to produce a swelling of the lattice [1,2,3]. The helium can be introduced either through implantation or in the case of tritides it is introduced via the radioactive decay of the tritium. The goal of the present study is to use large-scale atomistic simulations to investigate this process. In particular, the swelling associated with the introduction of helium and the resulting pressures in the bubble are evaluated. In addition, the nature of the defects produced during the bubble growth is examined. One of the values of atomistic simulations is that one can examine in detail the resulting defect structure. This work represents a continuation of earlier atomistic studies [4] that looked at the growth of a single small bubble. The current work is motivated by the ability to consider more realistic bubble densities and sizes and to consider systems with multiple bubbles.

There are numerous previous theoretical and experimental studies of helium bubble growth in the past [1,2]. Wolfer and co-workers examined the requirements for bubble growth via dislocation loop-punching mechanisms [1,6]. In these models the energetics associated with the growth of the helium bubble via the emmision of a prismatic dislocation loop are analyzed. This model provides a prediction of the bubble pressures required for bubble growth. These treatments assume the dislocation loops are retained after they are created via the punching process. This assumption leads to the prediction that in arrays of bubbles, the bubble pressure will initially decline as the bubbles grow but will then rapidly increase with further bubble growth. The rapid increase reflects the repulsive interaction between the existing dislocation loops between the bubbles and new loops that must be formed for further bubble growth. More recently, a growth model has been proposed by Chrzan and Wolfer[7] which considers the possibility of growth via dislocation pipe diffusion. This model postulates that in a bubble array dislocations segments will connect the bubbles. Thus a crucial question exists as to the nature of the dislocation structures that are produced during the bubble growth process. This issue will be addressed in the present work.

In this paper, the growth of a helium bubble array will be examined using atomistic computer simulations. The swelling and bubble pressures associated with the growth will be monitored. The swelling predictions are then compared to experimental observations of swelling in order to assess the validity of the simulations. Most importantly, the evolution of the defect structure between the bubbles will be analyzed and compared to the assumptions made by the existing continuum level descriptions of the bubble growth.

Computational Approach:

The basic approach employed in this paper is to perform an explicit molecular dynamics (MD) simulation of the bubble growth process. In this approach the dynamics of the bubble growth process are followed at the atomic scale. There are two advantages of this approach. First, the detailed mechanism associated with the growth process does not have to be assumed. The mechanism falls out of the simulation of the collective atomic

motion. The other advantage is that the results can be analyzed in greater detail than in experiment. Since the simulations have all of the atomic positions, it is possible to analyze the evolution is great detail. The intent is to use the qualitative understanding of the evolution of the defect structure in future work to motivate the development of appropriate continuum level descriptions of the bubble growth process.

There are also a couple of limitations to this simulation method that need to be kept in mind. These are related to the length and time scales at which these simulations are performed. For simulations over long times as will be needed here, computational limitations restrict the size of the system to on the order of a million atoms. For a cube of material in a fcc lattice, this corresponds to a cube of material a little under 25 nm on a side. Since a typical interbubble spacing in a metal tritide is on the order of 12 nm [8], the simulations will only be able to hold a small number of bubbles, for example 4. The other limitation is the time scale of the simulations. Again computational resources limit the time scale to the order of several nano-seconds. This is sufficient if the processes of interest are mechanically driven or athermal as is suspected in this case. However, if the actual mechanism depends on thermally activated events, the simulations may miss those processes.

The molecular dynamics simulations require a description of the interatomic interactions. The approach used here is the embedded atom method (EAM). This approach has been widely used to study the thermal and defect properties of late and nobel transition metals. This approach is described in detail and various applications are reviewed by Daw, Foiles and Baskes [9] and by Foiles [10]. In addition, reviews by Carlsson [11], by Raeker and DePristo [12] and by Nørskov [13] compare this approach to other similar approaches. The EAM potentials have the advantage of incorporating some of the dominant characteristics of metallic bonding while maintaining computational efficiency that is similar to that of simple pair interaction models. In the current study, new EAM potentials for Pd were used. Prior potentials were deficient in the description of the stacking fault energy. This is a key quantity for the structure and motion of dislocations that presumably will be an important aspect of the bubble growth process. The details of the EAM energy expression and the details of the Pd potentials used here are given in Appendix A.

The molecular dynamics are performed using standard algorithms that have been implemented into the code PARADYN by Plimpton [14,15]. This code is a parallel version of the serial code DYNAMO developed by Foiles and Daw [9]. These codes were written separately and cross-comparisons between the codes have been performed to verify the reliability of the codes. The simulations are performed at constant temperature and constant external pressure. The temperature is controlled via explicit rescaling of the velocities. The pressure is controlled using the method due to Paranello and Rahman [16]. These standard techniques allow the simulations to be performed in the constant NPT or isobaric-isothermal ensemble. Small-scale initial simulations were performed on various desktop workstations. The large-scale simulations were performed on ‘Janus’, the ASCI teraflop computer.

The current work focuses on the growth of inert gas bubbles in Pd. The method of the introduction of the inert gas will not be directly simulated. He is known to diffuse rapidly through the bulk metal lattice until it reaches a trapping site [4]. In the current simulation, the trapping sites are the bubbles forming in the lattice. Thus the He can be considered to be added directly to the bubble since it spends a negligable time in the lattice compared to the aging time of the real physical system. The first and most direct way to simulate the bubble growth is to add He atoms regularly to the bubbles and let the system evolve. This is the approach that was used in the earlier studies [4]. This approach has the advantage of making few assumptions about the resulting shape of the bubble and also provides a direct way to determine the pressure in the bubble.

The disadvantage of this approach is that it is impractical for the study of large bubbles. The range of helium content in the metal that is of interest goes to 40-50% helium to metal. As discussed above, the simulation cell will need to contain on the order 10^5 to 10^6 metal atoms and so will have to contain about half that number of helium atoms at the end of the simulations. Prior experience on the growth of helium bubbles by the direct addition of atoms [4] indicated that one needs several picoseconds (10^{-12} sec) for the system to relax from the addition of a single atom. This would require a simulation of hundreds of nanoseconds. That is unfeasible even with teraflop computing resources.

An alternate method of studying the evolution of the metal due to bubble growth has been developed. The key point is that the dense inert gas acts like a nearly incompressible inclusion in the metal. The presence of such an inclusion can be simulated by imposing a repulsive external potential on the metal atoms in the lattice that exclude the metal atoms from a spherical region. The growth of the bubble is modeling by the expansion of the volume inside of the repulsive potential. This approach has the appealing feature that the detailed dynamics of the inert gas atoms inside of the bubble does not need to be followed explicitly. This detailed behavior should have no effect on the response of the metal lattice except to determine the equation of state of the high density helium. The pressure in the bubble can be determined from the force exerted by the external potential on the metal atoms. Given the pressure and temperature in the bubble, the density of inert gas can be determined from the known equation of state of He. Given the volume of the inclusion and the inert gas density, the equivalent number of helium atoms in the bubble can be determined. In this manner, the bubble pressure and defect microstructure of the metal can be determined as a function of the helium content during the course of the simulation. The details of this procedure are described in Appendix B.

In order to assess the validity of this approach, small simulations were performed for the growth of helium bubbles in Ni. The simulations were performed in two ways. In the first simulation, the bubble growth was performed via the sequential addition of He atoms. In the second simulation, the bubble growth was performed via the repulsive potentials. In Figure 1, a slice of the metal lattice from both simulations is presented. Note that the helium atoms are not shown in the second and that the bubble is larger in thesecond case. The important point is that the qualitative nature of the atomic arrangements in the metal surrounding the bubble is the same in both cases. The mail feature is the rectangualr array of faults that surround the bubble. In both cases, th bubble

is surrounded by prismatic dislocation loops. This establishes the validity of the bubble growth approach that will be used below.

The results to be discussed were obtained from the simulation of two systems. The first system is a smaller system containing one bubble per periodic unit cell. The simulation cell started with 32,000 metal atoms. The system is periodic in all directions with sides of length 20 a_0 = 77.8 Å which yields a cell volume of 4.71 x 10^{-19} cm^3. Since there is a single bubble in each cell, the total initial bubble density is 2.12 x 10^{18} cm^{-3}. This is somewhat larger than the typical experimental density of bubbles in metal tritides. Since the periodic cell is cubic with one bubble, the system simulated actually represents a simple cubic lattice of bubbles in the material.

A second more realistic system was also simulated. The simulation cell started with 256,000 metal atoms. This is a cubic fcc lattice with sides of length 40 a_0 = 155.6 Å. The total initial volume of the cell is therefore 3.77 x 10^6 $Å^3$ = 3.77 x 10^{-18} cm^3. Four bubbles are introduced into this cell. This gives a total initial bubble density of 1.06 x 10^{18} cm^{-3} which is a realistic bubble density for metal tritides. The bubbles are located in an approximately fcc supercell arrangement within the cubic cell. The positions of the bubbles are displaced by a few percent from the ideal fcc supercell arrangement. The choice of a fcc arrangement was made to give a close-packed array of bubbles. The small deviation of the bubbles from this arrangement was to avoid artifacts that might result from an artificially high symmetry of the bubble arrangements. The bubbles each have the same size during the course of the bubble growth. The simulations are performed with periodic boundary conditions in all three directions. Thus the simulations represent a periodic array of bubbles.

Results:

The simulations of bubble growth were carried out till the number of He atoms per metal atom (He/M) ratio reached about 0.58 for the case of the small bubble system and about 0.39 for the case of the large system. Figure 2 presents a plot of the bubble pressure as a function of the inferred He/M ratio for the small system, the large system and the two combined. The bubble pressure is initially quite high (in excess of 200 kilobars) and then drops with time and increasing bubble size to the range of 30-40 kilobars. Unlike some earlier predictions [6], the bubble pressure is not observed to increase at high He/metal ratios. The values of the bubble pressures for the two systems are very similar, though there is a systematic difference in that the larger system, which has a lower overall density of bubbles, has somewhat smaller bubble pressures.

The computed pressure has strong fluctuations on two different time scales. This can be seen in Figure 3 which plots the pressure as a function of the simulated time. There is a very rapid fluctuation of ±5 kilobars. This reflects the thermal fluctuations inherent in all molecular dynamics simulations of pressure. There is another longer time-scale type of variation that gives the curves a somewhat saw tooth appearance. This is believed to be a result of discrete events in the relaxation of the bubble. In particular, the bubble pressure increases until there is a structural relaxation event that causes the system to relax and

lower the bubble pressure. This event is assumed to be the emission of dislocation loops, though this has not been observed directly in the simulation.

Another way to view the bubble pressure data is as a function of bubble radius. In Figure 4, we plot the product of the bubble pressure times the bubble radius as a function of the bubble radius. This choice of form is motivated by suggestions that the bubble pressure will scale inversely with the bubble radius as will be discussed below. In that picture, this plot should be roughly constant. In fact, there is a range of radii for which the product of P*R fluctuates around 13,000 – 14,000 ergs/cm^2. It then drops somewhat for larger values.

The simulations are performed at constant zero external pressure. Thus the volume of the computational cell increases as the bubbles grow. Tracking the cell volume as a function of the inferred He/M ratio allows for the determination of the swelling. The swelling is of interest for a variety of reasons. One issue associated with the swelling is the blistering that can occur in the vicinity of He implantation. Swelling is also of interest because it can be measured experimentally for the case of tritides. This provides a means of validating the predictions of the modeling.

The swelling associated with the bubble growth for the large system is shown in Figure 5 as a function of inferred He/M ratio. The swelling is given by $S = (V-V_0)/V_0$ where V is the current volume of the system and V_0 is the original volume in the absence of the bubbles. Note that the swelling again has the jagged structure that was also seen in the bubble pressure. It is also important to note that the swelling does not increase linearly with the helium content. This reflects the reduction in pressure of the helium bubbles with growth and the corresponding increase in the volume associated with each helium atom. The plot also includes a fit of the swelling data to a quadratic polynomial. The fit polynomial is

$$S = 0.6796x + 0.7662x^2$$

where S is the swelling defined above and x is the He/Metal ratio.

.

The final type of information that can be obtained from the simulation is insight into the defect structure that evolves during the bubble growth. This is important for the future development of continuum models. One of the advantages of the simulation is that it allows one to examine the defect structure in greater detail than is possible with experiment. A significant challenge in the analysis of the defect structure is the data reduction. In particular, the visualization of the defect structure is challenging since simply imaging the atomic structure does not allow one to see the defects. The large regions of perfect crystal obscure the defects. In order to visualize the defect structure, it is therefore important to be able to identify those atoms that are in perfect crystal environments and those that are in local defect environments. Here we use the centrosymmetry parameter first introduced by Kelchner, Plimpton and Hamilton [18]. This parameter measures the degree to which the nearest neighbor environment of a given atom is locally a center of inversion symmetry. The determination of this parameter is described in Appendix C. This parameter will vanish in a perfect fcc crystal

due to the inversion symmetry of the lattice and will continue to vanish for the case of uniform strain. The quantity becomes non-zero at structural defects including surfaces, planar faults, dislocation cores, and point defects. Substantial insight into the defect structure can be gained by just visualizing those atoms which have a value of the centrosymmetry parameter above a cut-off value.

Figure 6 shows the defect structure fairly early in the bubble growth process when the He/Metal ratio was about 0.04 in the large cell case. There are two views of the structure shown. In a), the shading is based on the value of the centrosymmetry parameter. In b), the shading represents the position of the atoms normal to the page of the view. In this figure, one sees three types of defect structures in addition to the atoms surrounding the bubble. (The atoms at the surface of the bubble do not have inversion symmetry and so have non-zero values of the centrosymmetry parameter.) First, there are some small isolated clusters of defected atoms. More detailed analysis of the structure of these clusters reveals that they are associated with lattice vacancies. The centrosymmetry parameter will be non-zero for each of the nearest neighbors of the vacant site. Second, there are close-packed planes of atoms immediately adjacent to the bubbles. This is particularly evident for the bubbles at the bottom of the figure. These structures represent dislocation loops created by the growth of the bubble. Finally, there are long filamentary structures extending away from the bubbles. These have been identified as dislocations.

Figure 7 shows the defect structure at a much later stage around He/M ~ 0.4. Note that the bubbles, which are identified by the atoms near the surface are much larger. In this case, one no longer sees the flat dislocation loops around the perimeter of some of the bubbles as was seen at the earlier stages of bubble growth. There are a significant number of small clusters of defected atoms. These are associated with point defects in the lattice. There is also what appears to be a stacking fault tetrahedron in the upper left corner of the image. The main other defect structures seen are dislocations that thread between the bubbles.

Discussion

The helium bubble pressures predicted in the current simulations are in reasonable accord with experimental investigations. Determinations of the density of helium in bubbles in a variety of metals has been reviewed by Donnelly [1]. The values of the helium densities reported are in the range of a 10^{22} cm^{-3} to 4 x 10^{23} cm^{-3}. Assuming a bulk equation of state, these densities correspond to pressures ranging from about a kbar to over 1000 kbar. The pressures determined here are within this broad range. There is a determination of He bubble pressure for bubbles in Pd tritides performed by Abell and Attalla [24]. These measurements used NMR techniques to observe the temperature of the helium melting transition and from this deduce the corresponding He bubble pressure. The experiments were performed on palladium tritide that had been aged for about one year and so had a He/M =0.03. They observed a range of bubble pressures from 60 – 110 kbar. This is completely consistent with the pressure computed here for these small values of the He/M ratio.

Continuum models of the bubble growth would benefit from a simple expression for the bubble pressure. Trinkhaus [25, 1] has proposed a very simple expression for the pressure of moderate size bubbles. His proposed expression is

$$P = \frac{2\gamma + \mu b}{R} \ .$$

In this expression, γ is the surface energy of the bubble, μ is the shear modulus of the metal and b is the burger's vector of the assumed prismatic loop. The results presented above show that the product of the the bubble pressure with the bubble radius is roughly constant over a range of bubble radii up to around 35Å. The value is in reasonble accord wth the expression due to Trinkhaus. If one assumes that the surface energy of the bubble is the same as the free surface energy of Pd, than 2γ = 4000 ergs/cm^2. If one take the shear modulus to be the Voight average shear and the Burger's vector to be that appropriate for a prismatic loop, than μb = 12,000 ergs/cm^2. This gives a total value of 16,000 ergs/cm^2 which is 15% higher than the values obtained in the simulations. Given the simplicity of the model, this is good agreement suggesting that the Trinkhaus expression is a useful simple result for estimating bubble pressure.

The swelling of pure metals due to the introduction of He cannot be readily observed experimentally. However, the swelling of metal tritides has been measured for a variety of metals. In metal tritides, the radioactive decay of the tritium introduces He into the lattice. If the tritide is aged under a constant overpressure, then the tritium content of the tritide is constant and the volume change of the sample is associated with the swelling due to the growth of He bubbles in the lattice. This swelling can be compared to the swelling computed here if one assumes that the deformation mechanism is not qualitatively changed between the metal and hydride. Since the underlying crystal structures of the metal atoms are the same in both cases, this is not an unreasonable assumption. To quantitatively compare the swelling, one needs to account for the fact that the lattice constant of the hydride phase is larger than that of the pure metal. Here we will make the simplest correction for that effect. The change in volume associated with a given He/M ratio will be taken from the calculations described above. The initial volume, though, will be assumed to be that of the hydride phase as opposed to the pure metal phase. This should capture the main difference in the swelling between the two materials.

The swelling predicted for the tritide based on the calculations for the large system with the above correction for the hydride volume difference is plotted in Figure 8. This plot also contains experimental results for the swelling of palladium tritide. The data for the lower values of He/M is based on length change measurements of palladium tritide performed by Guthrie. [7,23]. The other measurements are from NMR determinations of the He density by Abell [21,22]. Note that the NMR and length change measurements are in reasonable agreement at low values of He/M where both data exists. It is encouraging that the current swelling estimates are in good agreement with the experimental measurements especially considering the simplicity of the correction from the results for the pure metal to the hydride. It is particularly important to note that the swelling rate increasing as the He/M increases both for the experimental data and for the simulation results. This reflects the reduction in the average He bubble pressure that is

predicted in the simulations. The lower bubble pressure implies lower He density in the bubbles and so more swelling required to accommodate the He. Thus the observed upturn of the experimental swelling curve confirms the qualitative behavior of the computed bubble pressure. It is also important to note the comparison of the experimental data and the current results with the predictions of the early loop punching model of Wolfer [3,6] which is also plotted on Figure 8. That work predicted a swelling that is roughly linear in He/M with a slight reduction in the swelling rate at high He/M. This reflects the prediction of this early model that the He bubble pressure would rise at higher He/M. The current results and experiment are in disagreement with this prediction.

The prediction of the microstructure that results from the growth of the helium bubbles is an important aspect of the current results. The present results indicate that a dislocation network should form between the bubbles at least for the case of a dense bubble array. The present results also indicate that one does not accumulate a large number of prismatic loops between the bubbles as was envisioned in some of the earlier modeling work of Wolfer [6]. These results are not inconsistent with experimental observations of bubble growth in metals. There have been TEM observations of prismatic dislocation loops punched from bubbles in V [19,26]. However, the prismatic loops were only observed for low densities of bubbles. For high densities of bubbles, a dislocation network was observed near the bubbles. In a recent experimental study of Pd alloys [27], a large number of defects were observed in the first three months. These defects were interpreted by the authors as being due to a high density of dislocations and to large numbers of clusters of self-interstitial atoms. In particular, these observations did not see the retention of prismatic loops for this case of bubble growth in a palladium tritide.

Summary:

These simulations have examined the response of a metal lattice to the growth of a dense array of inert gas bubbles. The bubble densities considered here are similar to those observed to form due to the aging of metal tritides. The pressure of helium in the bubble is predicted to decrease monotonically with increasing helium to metal ratio. The magnitudes of the pressure are in accord with various experimental estimates of the bubble pressure in metal tritides. The swelling of the metal due to the tritides is also predicted. The rate of swelling is computed to increase with increasing helium to metal ratio consistent with experimental observations on the swelling of metal tritides. The detailed defect structure resulting from the bubble growth is observed. It is found that a dislocation network forms that connects the bubbles. This is contrary to some early assumptions by Wolfer [6] that prismatic loops would form and be retained between the bubbles. It is consistent, though, with a later suggestion by Chrzan and Wolfer [7] that dislocation pipes will connect the bubbles. This in turn suggests that their pipe difusion model deserves further study.

References:

1. S. E. Donnelly, “The Density and Pressure of Helium in Bubbles in Implanted Metals: A Critical Review”, Radiation Effects **90**, 1-47 (1985).
2. *Fundamental Aspects of Inert Gases in Solids*, edited by S. E. Donnelly and J. H. Evans (Plenum Press ,New York, 1991).
3. W.G. Wolfer, B.B. Glasgow, M.F. Wehner and H. Trinkhaus, J. Nucl. Mater. **122-123**, 565 (1984).
4. J. B. Adams, W. G. Wolfer, S. M. Foiles, C. M. Rohlfing, and C. D. van Siclen, "Theoretical Studies of He in Metals", in Proceedings of NATO Workshop on Fundamentals Aspects of Inert Gases in Solids, ed. S. E. Donnelly and J. H. Evans, (Plenum Press, 1991).
5. W. G. Wolfer, “The Pressure for Dislocation Loop Punching by a Single Bubble”, Phil. Mag. A**58**, 285-297 (1988).
6. W. G. Wolfer, “Dislocation Loop Punching in Bubble Arrays”, Phil. Mag. A**59**, 87-103 (1989).
7. D. C. Chrzan and W. G. Wolfer, “Helium Bubble Growth by the Dislocation Pipe Mechanism”, Sand report 91-8671.
8. G. J. Thomas and J. M. Mintz, J. Nucl. Materials **116**, 336 (1983).
9. M. S. Daw, S. M. Foiles and M. I. Baskes, “The Embedded Atom Method: A Review of Theory and Application”, Materials Science Reports **9**, 251-310 (1993).
10. S. M. Foiles, “Atomistic simulations of surfaces and interfaces”, in *Equilibrium Structure and Properties of Surfaces and Interfaces*, edited by A. Gonis and G. M. Stocks (Plenum Press, New York, 1992).
11. A. E. Carlsson, in *Solid State Physics*, edited by H. Ehrenreich, H. Seitz and D. Turnbull, vol 43 (Academic Press, New York, 1990).
12. T. J. Raeker and A. E. DePristo, International Reviews in Physical Chemistry 10, 1 (1991).
13. J. K. Nørskov, Reports on Progress in Physics 53, 1253 (1990).
14. S. J. Plimpton and B. A. Hendrickson, “Parallel Molecular Dynamics with the Embedded Atom Method”, SAND93-0260C
15. S. J. Plimpton and B. A. Hendrickson, “Parallel Molecular Dynamics with the Embedded Atom Method”, in *Materials Theory and Modeling*, edited by J. Broughton, P. Bristowe and J. Newman (Materials Research Society, Pittsburgh, 1993).
16. M. Parrinello and A. Rahman, “Crystal Structure and Pair Potentials: A Molecular-Dynamics Study”, Phys. Rev. Lett. **45**, 1196 (1980).
17. R. L. Mills, D. H. Lievenberg and J. C. Bronson, Phys. Rev. B**21**, 5137 (1980).
18. C. L. Kelchner, S. J. Plimpton, and J. C. Hamilton, Phys. Rev B**58**, 11085 (1998).
19. W. Jager, R. Lasser, T. Schober, and G. J. Thomas, Radiation Effects **78**, 165 (1983).
20. G. J. Thomas, Radiation Effects **78**, 37 (1983).
21. G. C. Abell, in *Fundamental Aspects of Inert Gases in Solids*, edited by S. E. Donnelly and J. H. Evans (Plenum Press, New York, 1990).
22. G. C. Abell and D. F. Cowgill, Physical Review B**44**, 4178 (1991).
23. S. E. Guthrie, unpublished.
24. G. C. Abell and A. Attalla, Physical Review Letters **59**, 995 (1987).

25. H. Trinkhaus, Radiation Effects **78**, 189 (1983).
26. T. Schober, R. Lässer, W. Jäger and G.J. Thomas, J. of Nuclear Materials **122&123** 571 (1984).
27. S. Thiébaut, B. Décamps, J.M. Pénisson, B. Limacher and A. Percheron Guégan, J. of Nuclear Materials **277**, 217 (2000).
28. M. S. Daw and M. I. Baskes, "Embedded-atom method: Derivation and application to impurities, surfaces and other defects in metals", Phys. Rev. B**29**, 6443 (1984).
29. S. M. Foiles, M. I. Baskes and M. S. Daw, "Embedded-atom-method functions for the fcc metals Cu, Ag, Au, Ni, Pd, Pt, and their alloys," Phys Rev B 33, 7983 (1986).
30. A. F. Voter and S. P Chen, Materials Research Society Proceedings vol. **82**, 175 (1987).
31. S.M. Foiles, "Calculation of the surface segregation of Ni-Cu alloys with the use of the embedded-atom method", Phys. Rev. B**32**, 7685.

Appendix A:

New EAM potentials for Pd were developed for these simulations. There are two reasons why the existing potentials for Pd [28, 29] were not adequate. The stacking fault energies and the surface energies of the prior potentials are substantially too low. The stacking fault energy is a key parameter in determining the dislocation core structure and it was felt to be important to have correct dislocation structures since that is key to the deformation behavior of the material. The potentials were fit to the equilibrium lattice constant, the equation of state, the elastic constants, the vacancy formation energy, the intrinsic stacking fault energy and the surface energy. The functional forms for the fit followed the work of Voter and Chen [29].

The details of the potential are as follows. In the EAM [9], the total energy is expressed by the usual equation

$$E = \sum_i F_i\left(\sum_{j \neq i} f_j(R_{ij})\right) + \frac{1}{2}\sum_{ij, i \neq j} \phi_{ij}(R_{ij})$$

where i and j refer to atoms, R_{ij} is the separation of atoms i and j, f(R) is electron density function, F is the embedding function and ϕ is the pair interaction. The pair potential, ϕ, is expressed in a Morse potential form

$$\phi(R) = A\{[\exp(-\beta(R - R_0)) - 1]^2 - 1\}$$

with the parameter values A = 1.21433 eV, β = 0.79689 Å^{-1} and R_o = 2.21645 Å. The electron density function is given by

$$f(R) = B\{R^m \exp(-\gamma R) + 2^{m+3} R^m \exp(-2\gamma R)\}$$

with the parameter values B=1, m=8 and γ = 3.16413 Å^{-1}. Both of these functions are truncated at R_{cut} with the same procedure. A function of distance, g(R), is modified to

$$g(R) \rightarrow g(R) - g(R_{cut}) + \frac{R_{cut}}{n}\left(1 - \left(\frac{R}{R_{cut}}\right)^n\right) g'(R_{cut})$$

with n=20 and R_{cut} = 5.35 Å. Finally, the embedding function is determined numerically to obtain agreement with the equation of state of the solid as described in detail by Foiles [31]. For this reason the overall scale of the electron density function, f(R), is arbitrary. Thus the value of B was simply taken to be unity.

The properties that result from this fit are summarized in the following table. Note that both the surface and stacking fault energies are reproduced well in addition to good results for the elastic moduli and the vacancy formation energies.

	Desired	Fit
a_0 (Å)	3.89	3.89
E_{sub} (eV)	3.91	3.91
C_{11} (10^{12} ergs/cm^3)	2.341	2.392
C_{12} (10^{12} ergs/cm^3)	1.76	1.735
C_{44} (10^{12} ergs/cm^3)	0.712	0.656
E_{vac}^{form}	1.54	1.58
γ_{sf} (ergs/cm^2)	188	187
γ_{surf} (ergs/cm^2)	2000.	1958

Appendix B:

The external potential associated with the bubble i centered at the position $\vec{R}_i$ is defined as follows. The potential at R is determined in terms of a scaled distance from the center given by $d = \frac{\left|\vec{R} - \vec{R}_i\right| - R_B}{L}$ where $\left|\vec{A}\right|$ denotes the norm of the vector and R_B is the radius of the bubble. The potential is given by a cosine form for –1/2 < d < 0, namely,

$$V(d) = \frac{1}{2} V_0 (1 - \cos(\pi d)) .$$

For d>0, V(d) = 0 and for d< -1/2,

$$V(d) = \frac{1}{2} V_0 (1 - \pi (d + \frac{1}{2})) .$$

The parameter values L = 2 Å and V_0 = 25 eV were chosen here. Numerical experiments indicate that the results are not very sensitive to the exact choice of these parameters. The bubble radius is chosen to increase with the cube root of the time so that the bubble volume increases linearly with time. In particular, the bubble volume was chosen to increase at a rate of 25Å^3/ps = 25 10^{-12} cm^3/s.

The inert gas pressure is determined from the net force that is applied to the surrounding metal atoms. The normal force exerted by the external potential on all of the metals atoms is summed and then divided by the surface are of the bubble. This yields the net pressure inside of the bubble.

The pressure and temperature of the inert gas is then used to determine the density of the inert gas. For this purpose we use the empirical equation of state for helium developed by Mills, Liebenberg and Bronson [17] which is given by

$$V = (22.575 + 0.0064655T - 7.2645T^{-1/2})P^{-1/3} + (-12.483 - 0.024549T)P^{-2/3} + (1.0596 + 0.10604T - 19.641T^{-1/2} + 189.84T^{-1})P^{-1} .$$

In this expression, V is the molar volume in cm^3, P is the pressure in kilobars and T is the temperature in Kelvin.

Appendix C:

The centrosymmetry parameter is determined in a somewhat different manner here than in the original implementation of Kelchner, Plimpton and Hamilton [18]. The original implementation relied on knowledge of the position of the 12 nearest neighbors in a reference-undistorted lattice with the same orientation as the original crystal. These nearest neighbors in the reference lattice are group into pairs i and i+6 which have opposing nearest neighbor vectors. One then identified the atoms in the actual system which are closest to these reference neighbor positions and calculated the quantity $P = \sum_{i=1,6} \left| \vec{R}_i + \vec{R}_{i+6} \right|^2$. For a perfect fcc crystal, this sum will vanish since each term of the sum is zero. This implementation has the disadvantage that one must know the macroscopic orientation of the crystal and adjust the algorithm accordingly. This is a practical inconvenience. In addition, if there has been a local rotation of the lattice due to deformation, this algorithm may also fail.

The current algorithm computes a similar quantity, but it does not rely on a reference set of nearest neighbor vectors. The first step is to identify the set of 12 nearest neighbors of a given atom and the vectors, $\vec{R}_i$, to each of them. One then computes the value of $\left| \vec{R}_i + \vec{R}_j \right|^2$ for all 66 combinations of i<j. The six smallest values are then summed to obtain the centrosymmetry parameter. In the case of a perfect fcc lattice, six of the values will vanish which corresponds to the cases where i and j refer to opposing nearest neighbors. The advantage of the current implementation is that it does not require an *a priori* knowledge of the crystal orientation. In the vicinity of a defect, the centrosymmetry parameter will be non-zero. This includes any defect which local breaks to inversion symmetry of a site. This includes surfaces, stacking faults, dislocation cores and point defects to name a few possibilities.

Figure Captions:

Figure1. Comparison of the structure of obtained via the sequential addition of He atoms (a) with the structure obtained via an expanding repulsive potentia (b). See text for discussion. In a) the green atoms are the helium atoms whereas in b) the empty space represents the area that would be filled with helium. Note that the figures are for somewhat different bubble sizes. In both case, though, the same type defect structure surrounds the bubbles.

Figure 2. The He bubble pressure in kilobars as a function of the helium to metal (He/M) ratio for a) the small system, b) the large system and c) both systems. See text for the definition of the two systems.

Figure 3. The time dependence of the bubble pressure for a) the small system and b) the large system. The small time variations are typical MD variations of the pressure. The longer time sawtooth variations is assumed to reflect individual athermal relaxation events.

Figure 4. The product of the bubble pressure with the bubble radius as a function of the bubble radius for the larger system. (Less pressure data was recorded during the initial stages of the simulation which explains the lack of fine scale fluctuations in the initial portion of the curve.)

Figure 5. The computed swelling of the metal due to the growth of the He bubbles as a function of the inferred helium to metal ratio. The solid curve is a fit to the data.

Figure 6. View of the defect structures in the large system at a helium to metal ratio of 0.04. Only those atoms with a non-zero value of the centrosymmetry parameter (see text) are plotted. In a) shading is based on the value of the centrosymmetry parameter. The shading is a blackbody scale with brighter atoms being more defected. In b) the shading is based on the position of the atoms normal to the page with darker atoms in the back.

Figure 7. Same as Figure 6b except for a helium to metal ratio of 0.4.

Figure 8. Comparison of the predicted swelling adjusted to the case of a tritide (see text) compared with experimental estimates of the swelling. See text for references.

Figure 1

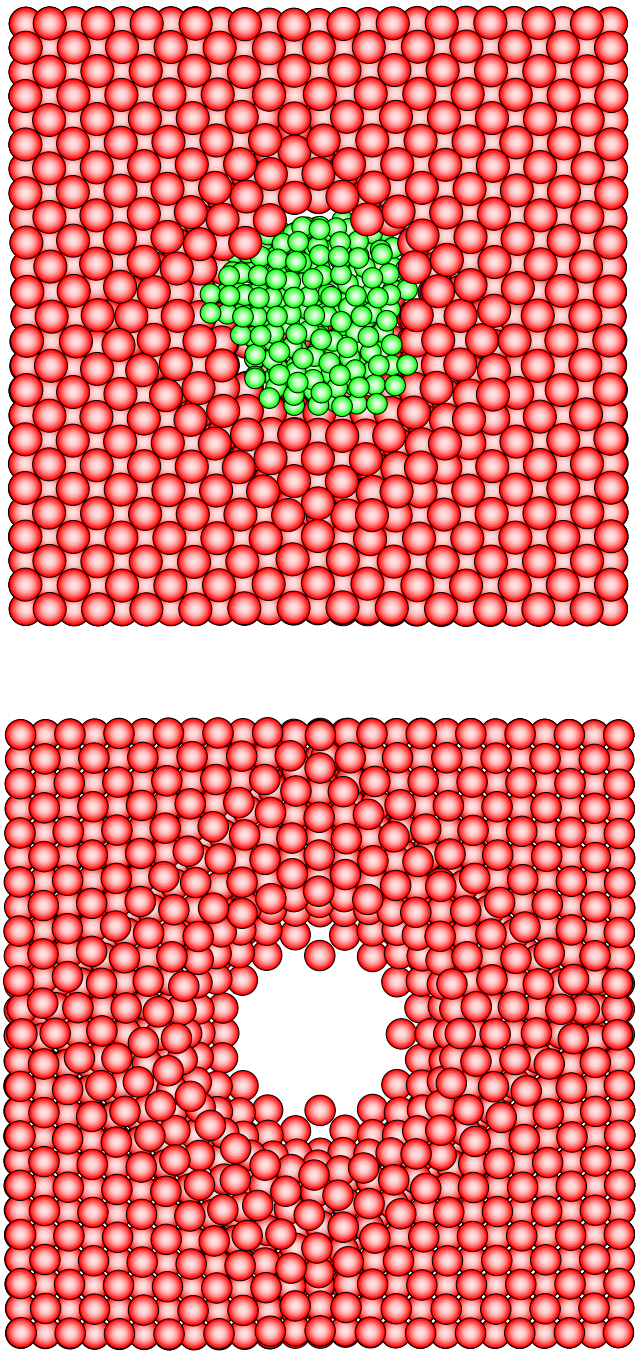

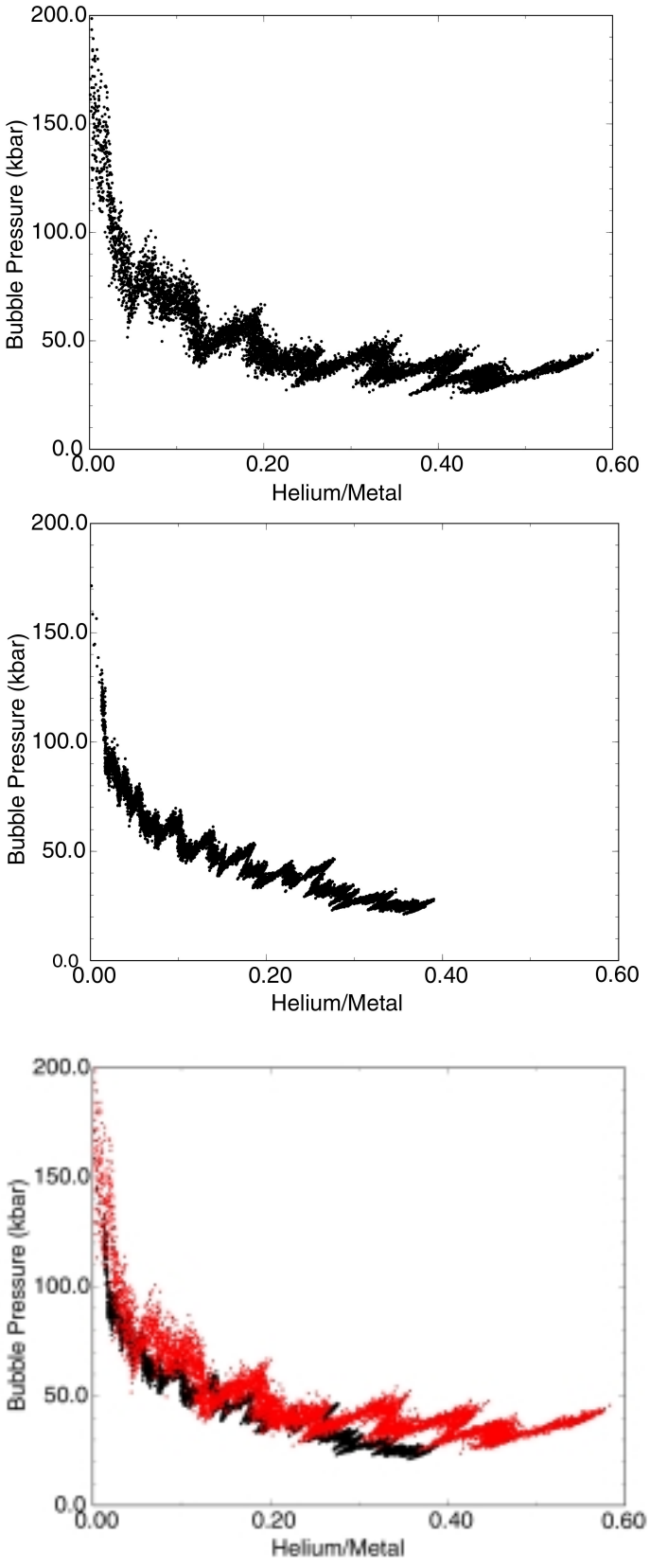
200.0
150.0
100.0
50.0
0.0
Bubble Pressure (kbar)
0.00
0.20
0.40
0.60
Helium/Metal

Figure 2

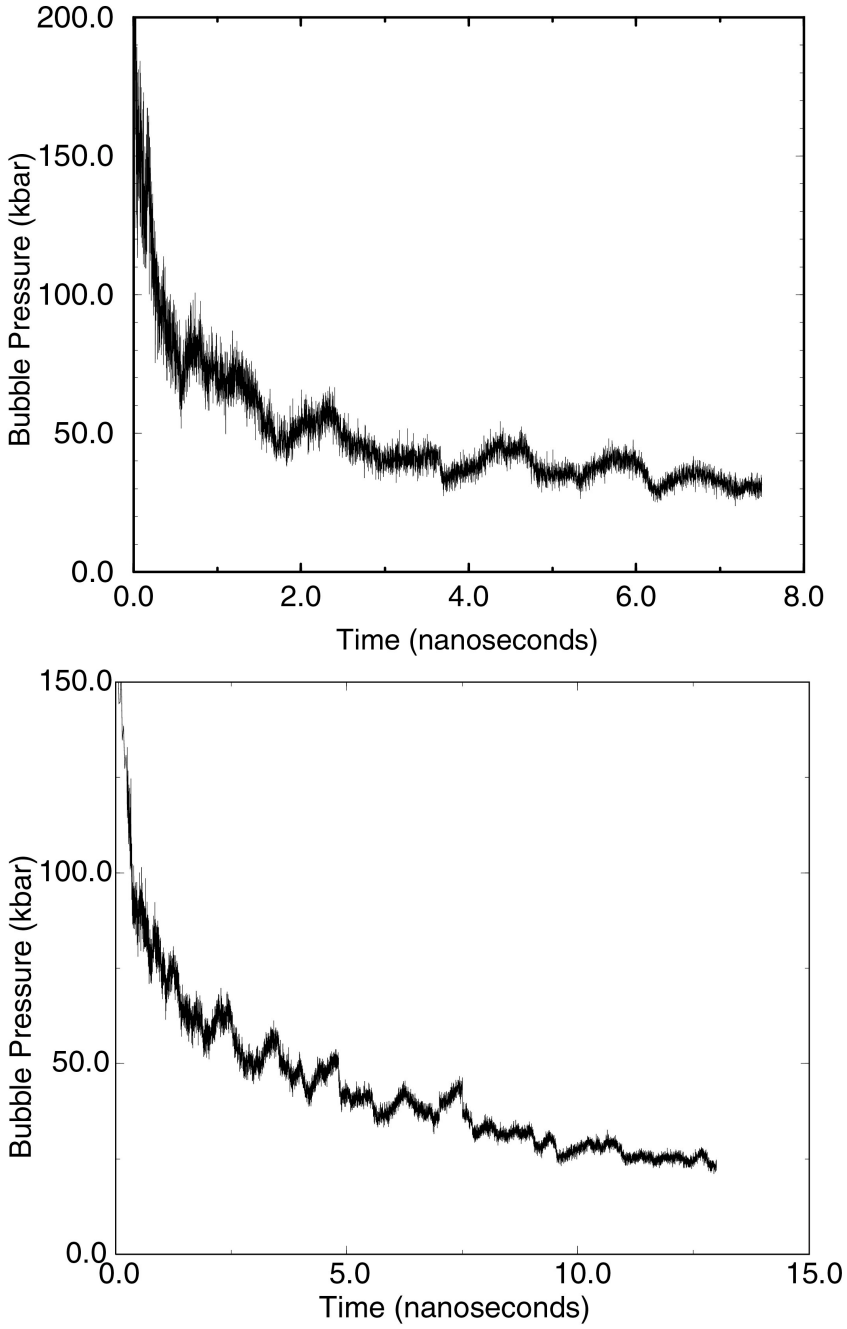
200.0
150.0
100.0
50.0
0.0
Bubble Pressure (kbar)
0.0
2.0
4.0
6.0
8.0
Time (nanoseconds)
150.0
100.0
50.0
0.0
Bubble Pressure (kbar)
0.0
5.0
10.0
15.0
Time (nanoseconds)

Figure 3

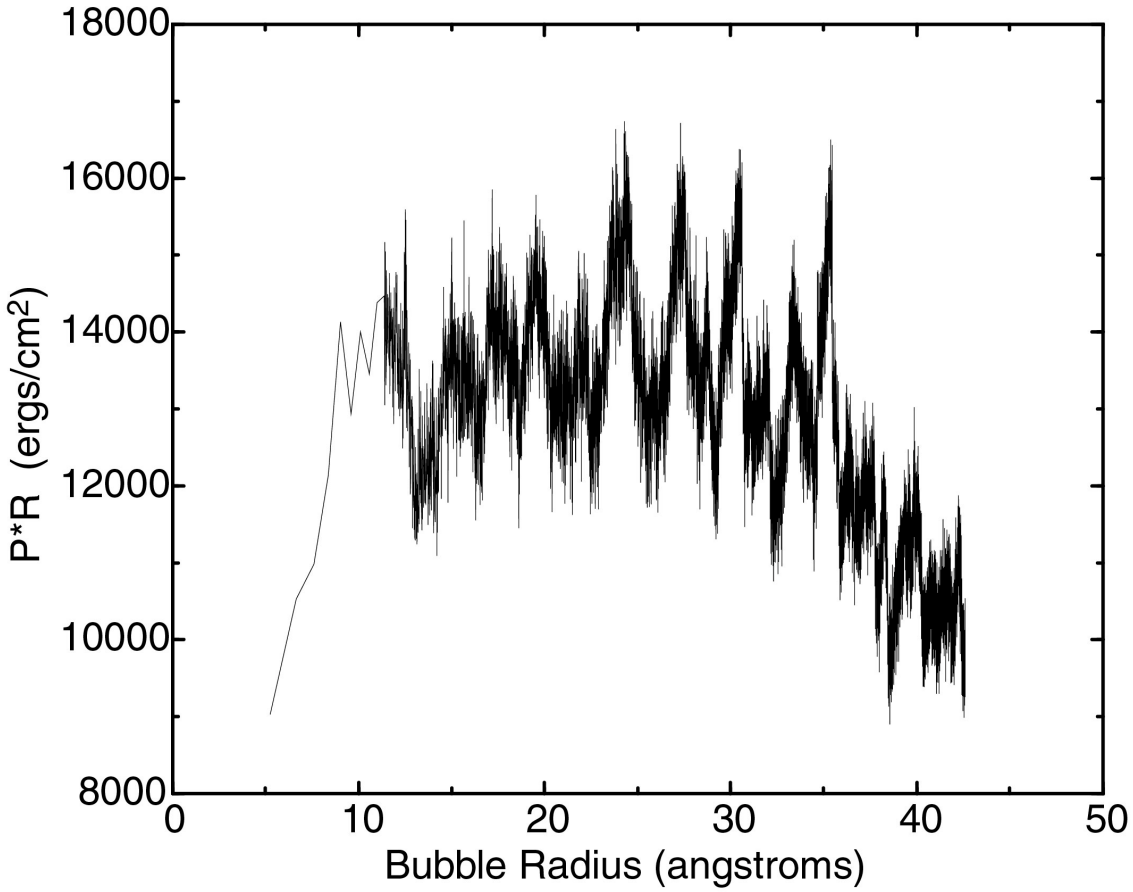
18000
16000
14000
12000
10000
8000
P*R (ergs/cm2)
0
10
20
30
40
50
Bubble Radius (angstroms)

Figure 4

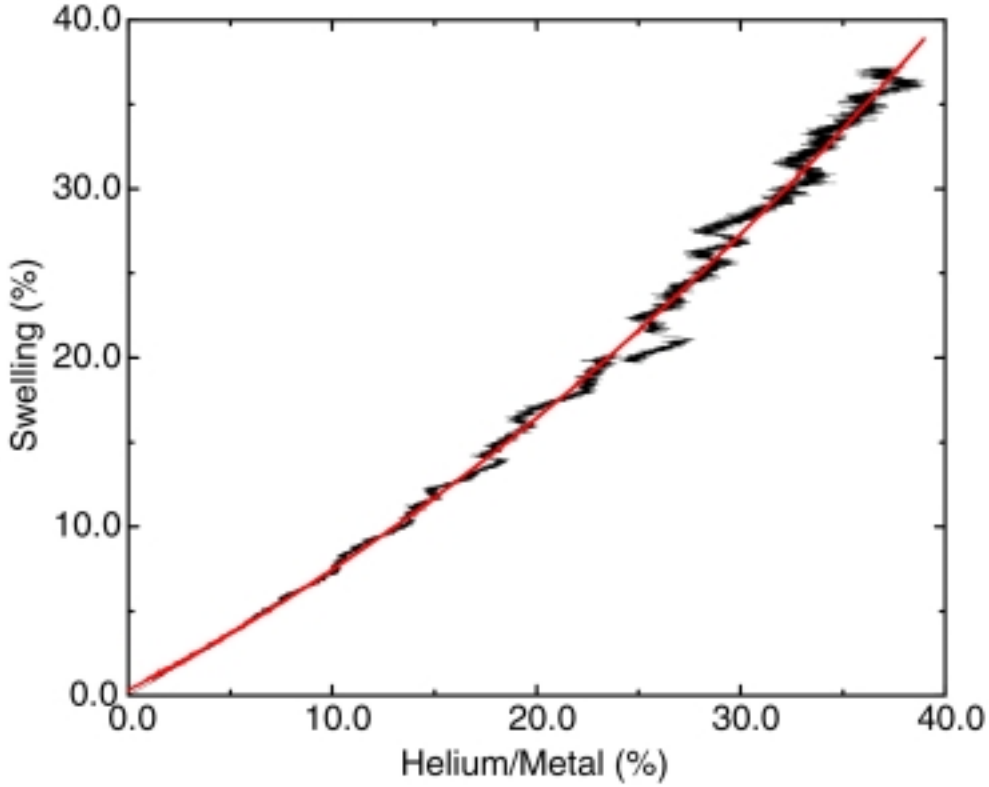

Figure 5

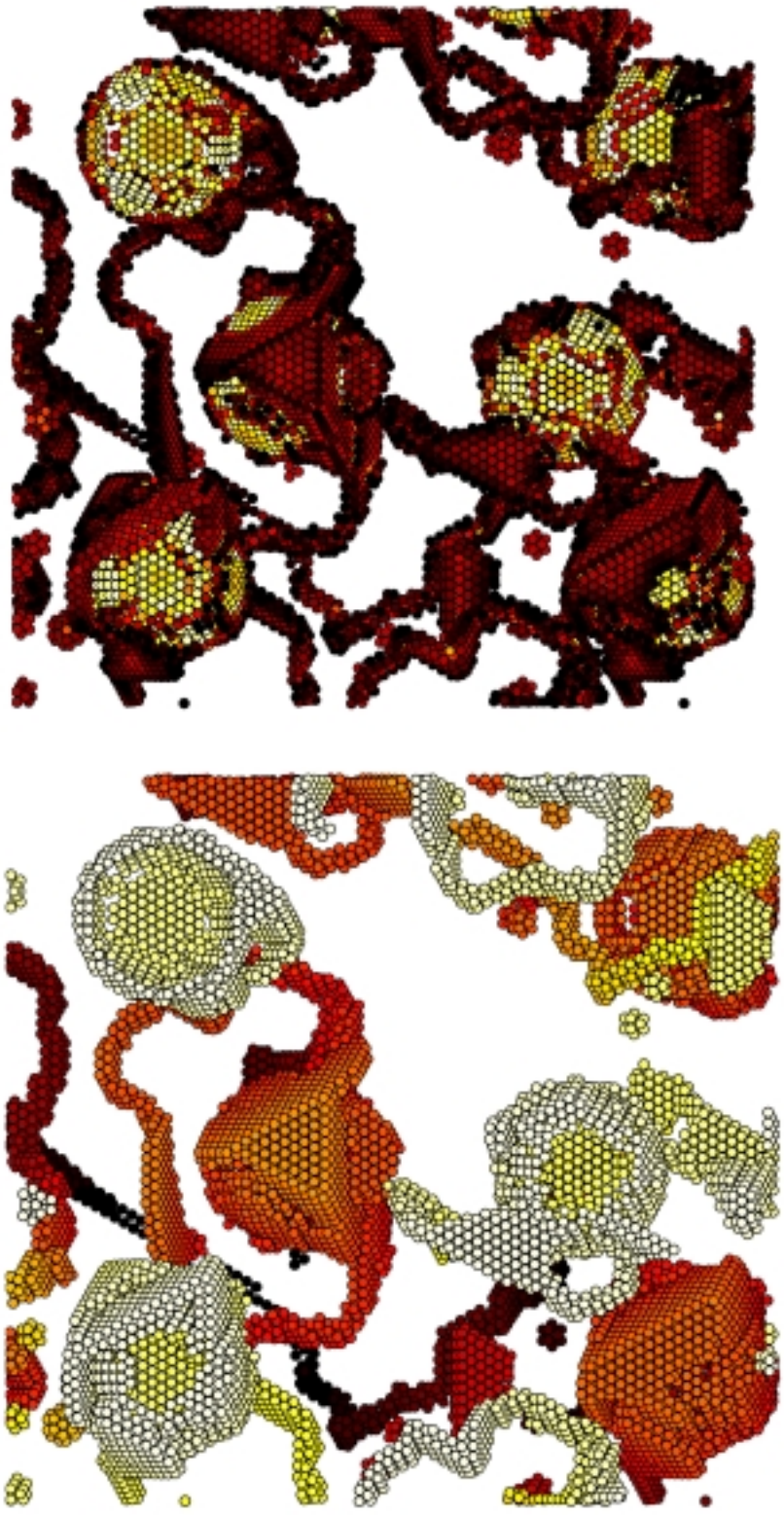

Figure 6

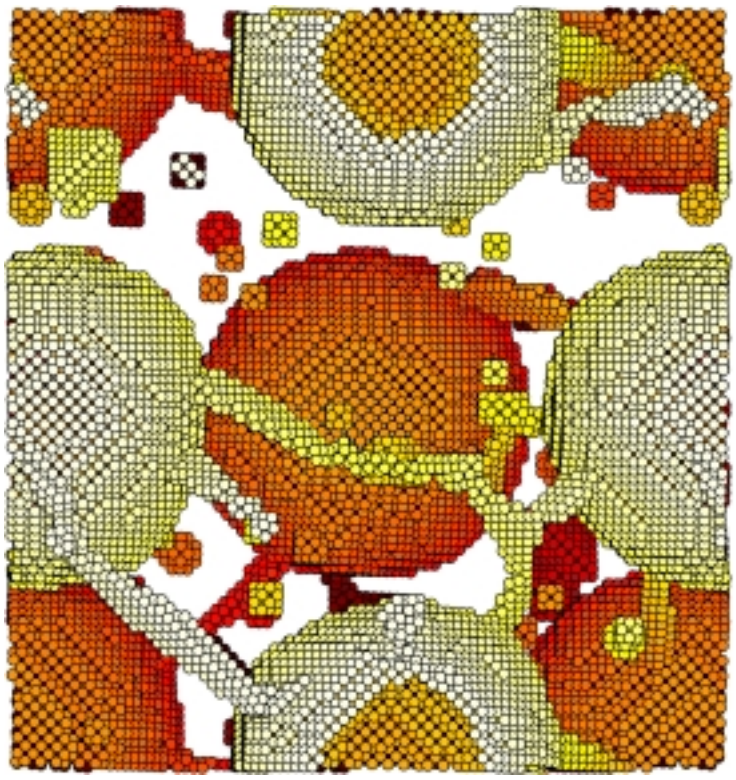

Figure 7

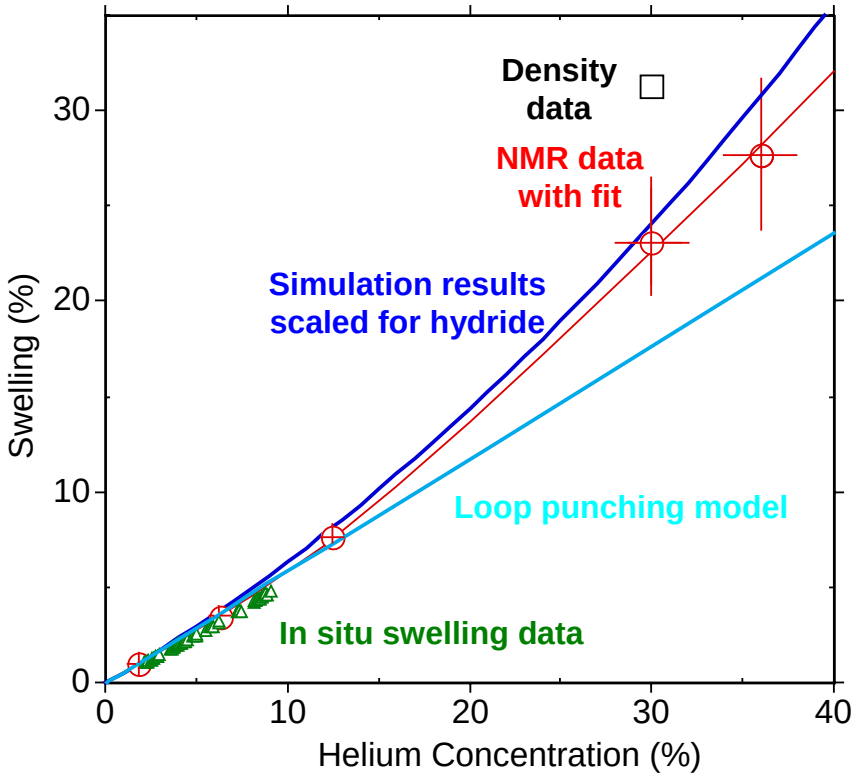
Density
data
NMR data
with fit
Simulation results
scaled for hydride
Loop punching model
In situ swelling data
Swelling (%)
Helium Concentration (%)
0
10
20
30
40

Figure 8

Distribution:

1	MS0316	Grant Heffelfinger, 9209
1	MS0819	Tim Trucano, 9211
1	MS0835	James Perry, 9121
1	MS0885	Julia Phillips, 1802
1	MS1411	H. Eliot Fang, 1834
5		Stephen Foiles, 1834
5		Jeff Hoyt, 1834
1	MS9108	G. Cook Story, 8414
1		Steve Robinson, 8414
1		Mike Hardwick, 8414
1		Carl Pretzel, 8414
1		Ray Baldonado, 8414
1	MS9161	Er-Ping Chen, 8726
1		Jonathan Zimmerman, 8726
1	MS9202	Rena Zurn, 8418
1	MS9402	Ken Wilson, 8722
1		Rion Causey, 8724
1		Don Cowgill, 8724
1		Kristen Hertz, 8724
1	MS9403	James Wang, 8723
1		Arlyn Antolak, 8723
1		Dan Morse, 8723
1	LLNL	Wilhelm Wolfer, L353
1		Seymour Sack, L170
1	LANL	Brad Meyer, G780
1		Johndale Solem, B210
1	MS9018	Central Technical Files, 8945-1
2	MS0899	Technical Library, 9616
1	MS0612	Review & Approval desk, 9612
		For DOE/OSTI